Dynamics of a coplanar-electrode plasma display panel cell. I. Basic operation

Shahid Rauf [a)] and Mark J. Kushner [b)]

Department of Electrical and Computer Engineering, University of Illinois, 1406 West Green Street, Urbana, Illinois 61801

Plasma display panels (PDPs) are a technology for large-area high-brightness flat panel displays. There is considerable interest in improving PDP efficiency by optimizing the cell design, input voltage characteristics, operating conditions and gas mixture. In this article, we report on a two-dimensional computer model for PDPs which has been used to investigate the operation of a coplanar-electrode PDP cell sustained in He/Ne/Xe gas mixtures. The plasma transport equations are implicitly integrated in time to enable simulation of complex gas mixtures and PDP cell designs. To resolve the details of the electron dynamics, the electron temperature is computed by solving the electron energy equation. A Monte Carlo simulation for secondary electrons and a radiation transport model for visible light emission are also employed. The basic operation of the PDP cell is described in this article. The first pulse was usually found to initiate a discharge between the top electrodes and the bottom address electrode, which was grounded. Only after a positive surface charge was formed on the bottom dielectric did the discharge shift to being between the coplanar electrodes. For our conditions, radiation from Xe_2^* made a larger contribution to exciting the phosphor for visible light emission than radiation from the resonance states of Xe since radiation from Xe_2^* is optically thin. © *1999 American Institute of Physics.* [S0021-8979(99)07107-8]

I. INTRODUCTION

Plasma display panels (PDPs) are one of the leading technologies currently under development for large-area high-brightness flat panel displays.[1–3] There is considerable interest in increasing the luminance of PDPs by improving PDP visible light generation efficiency.[1] This improvement will most likely result from a systematic optimization of the cell design, operating conditions, voltage pulse characteristics, and gas composition, an endeavor that can benefit from a detailed understanding of the dynamics of PDP cells. There are also concerns regarding the lifetime of PDPs, the extension of which may require design improvements that minimize ion bombardment on phosphors. To investigate these issues, we have developed a two-dimensional (2D) hybrid simulation for the direct-current (dc) pulsed plasma operation of PDP cells. The model has been used to simulate a coplanar-electrode PDP cell sustained in He/Ne/Xe gas mixtures. In this and a companion article,[4] we use results from these studies to describe the operation of the PDP cell under a wide variety of operating conditions. We specifically investigated the consequences of applied voltage magnitude, gas pressure, gas composition, cell dimensions and dielectric material on the ultraviolet and visible light generation capability and efficiency of PDP cells.

The invention of the alternating-current (ac) PDP device is generally attributed to Bitzer and Slottow.[5] During the 1970s, several companies including IBM developed neon-based monochrome flat panel PDPs while most of the current research focuses on color displays. Since it is difficult to formulate gas mixtures that efficiently produce the primary colors, color PDP cells generally use xenon gas mixtures to generate ultraviolet (UV) photons that are converted to visible light through phosphors. In a typical PDP cell, a noble gas mixture is sealed between dielectric materials that are backed by conducting electrodes. A discharge is initiated by applying a voltage pulse to the electrodes, which produces UV radiation which is subsequently converted to visible. Fluxes of ions and electrons to the dielectric surfaces charge the dielectric capacitance, which decreases the voltage across the gap and quenches the discharge. This process can be repeated indefinitely by applying voltage pulses of alternating polarity or the same polarity to opposing electrodes. The applied voltage on successive pulses can usually be less than the breakdown voltage since the charged capacitance of the dielectric from the previous pulse generates an electric field in the same direction as the applied voltage of the next pulse.

A number of computational studies have previously investigated PDP cell operation. Sahni and Lanza developed a one-dimensional (1D) fluid model[6] and demonstrated that the secondary electron emission from the dielectrics has a strong influence on the dynamics of a neon-based monochrome PDP.[7,8] Veerasingam, Campbell, and McGrath developed both 1D and 2D fluid models for PDPs[9–11] which were applied to the operation of He and He/Xe based opposing-electrode PDP cells. Their computed results qualitatively agreed with experiments. The quantitative discrepancies were attributed to uncertainties in the fundamental data base (e.g., electron impact cross-sectional data and secondary electron emission coefficients), the use of local field approximation and uncertain initial conditions in the experiments.

[a)]Present address: Motorola, Embedded Systems Technology Laboratory, 3501 Bluestein Blvd., Austin, TX 78721. Electronic mail: ra8952@email.sps.mot.com

[b)]Author to whom correspondence should be addressed. Electronic mail: mjk@uiuc.edu

Drallos, Nagorny, and Williamson developed a 1D kinetic PDP model[12] and an analytical model.[13] Their kinetic studies showed that the local field approximation does not adequately resolve the details in the cathode fall region. Boeuf, Pitchford, and Punset applied their 2D hybrid plasma code to the simulation of Ne/Xe gas mixtures in PDPs.[14,15] Their simulation of multiple opposing-electrode PDP cells showed that barrier ribs are essential for avoiding cross-talk between adjacent cells.

The current issues in PDP research deal with the optimization of the opposing-[16] and coplanar-electrode[17] cell designs having multicomponent gas mixtures to improve PDP efficiency and light emission characteristics. To investigate these issues, we developed a 2D hybrid simulation for PDPs. As in the previous studies, the basic physical model consists of the continuity equations for all species, Poisson's equation and an equation for dielectric surface charging. Except for the continuity equations for uncharged species, the coupled and nonlinear equations are implicitly integrated in time using the biconjugate gradient squared sparse matrix technique.[18] The continuity equations for neutral species are solved explicitly in time. Several methods have been implemented to compute electron transport coefficients and source functions for electron impact reactions. The simplest is the local field approximation (LFA) which was used in previous PDP models.[9-11,15,16] Alternatively, electron transport coefficients and electron impact reaction source functions can be determined in terms of the electron temperature, which is self-consistently computed by implicitly integrating the time dependent energy conservation equation. Secondary electron emission is taken into account either through a flux boundary condition in the electron continuity equation or a more detailed Monte Carlo simulation. Finally, a radiation transport model was implemented to determine the visible light output of the cell.

In this and the companion article, we focus our attention on a coplanar-electrode PDP cell using He/Ne/Xe gas mixtures. The basic operation of the device is described in this article. It is found that the first voltage pulse usually initiates a discharge between the top electrodes and the bottom address electrode, which is grounded. From the next pulse onward, the positive surface charge on the bottom dielectric shields the address electrode, and the discharge shifts to being between the two top electrodes. Even though the peak Xe_2^* density is considerably smaller than that of atomic Xe excited states, Xe_2^* contributes more strongly to the visible light emission through excitation of the phosphor. For our conditions this trend results from the short lifetime of Xe_2^*, UV radiation from Xe_2^* being optically thin, and Xe^* readily converting to Xe_2^* through three-body collisions. Use of the Monte Carlo simulation or electron energy equation do change the detailed dynamics of the discharge, but the overall characteristics are similar to those obtained with the local field approximation.

We describe the model in Sec. II. Section III contains a discussion of the basic dynamics of the PDP cell and key observations are summarized in Sec. IV.

II. DESCRIPTION OF THE MODEL

Our basic model consists of the fluid equations of continuity and momentum conservation for all species, the electron energy conservation equation, Poisson's equation, and an expression for dielectric surface charging. As the gas pressure in the PDP cells is usually high ($\sim$100 Torr), it was not found necessary to solve the momentum conservation equation *per se*. We instead used the drift-diffusion approximation, which considerably reduces the simulation time. Although a fluid approximation has been used for electrons to compute their density, flux, and temperature, we also implemented a Monte Carlo simulation (MCS) to more accurately represent the electron impact source functions due to secondary electrons.

The main simulation consists of integrating the following set of coupled equations:

$$\nabla \cdot (\epsilon \nabla \phi) = -\sum_{i=1}^{N_{ch}} q_i n_i - \rho, \tag{1}$$

$$\frac{\partial n_i}{\partial t} - \nabla \cdot (D_i \nabla n_i + (q_i/|q_i|) \mu_i n_i \nabla \phi) = S_i,$$

$$\text{for } i = 1, 2, \ldots, N_{ch}, \tag{2}$$

$$\frac{\partial \rho}{\partial t} = \sum_{i=1}^{N_{ch}} q_i \nabla \cdot (D_i \nabla n_i + (q_i/|q_i|) \mu_i n_i \nabla \phi),$$

$$\text{at dielectric surfaces}, \tag{3}$$

where ϕ, ρ, ϵ, n_i, D_i, μ_i, q_i, and S_i are the electrical potential, charge on dielectric surfaces, permittivity, and number density, diffusion coefficient, mobility, charge, and source function for species i, respectively. N_{ch} is the number of charged species. The source function includes collisional terms which locally change the species density, such as electron impact ionization. Due to dielectric relaxation, the maximum time step one can use for explicit time integration in typical PDP simulations during the discharge pulse is less than a picosecond. This makes the simulations impracticably slow for modeling complete discharge pulses (10 μs) in complex gas mixtures. As in Ref. 9, the approach we have used to overcome this time constraint is a fully implicit solution technique. The procedure consists of linearizing the nonlinear Eqs. (1)–(3) at each time step, and writing them in the form,

$$F(\mathbf{X}) \equiv \mathbf{A} \cdot \mathbf{X} - \mathbf{B} = \mathbf{0}, \tag{4}$$

where $\mathbf{A}$ is the Jacobian matrix, $\mathbf{B}$ is a vector that depends on plasma conditions during the previous time step, and $\mathbf{X}$ is the vector of unknown quantities. Newton's method is then used to solve for $\mathbf{X}$. During the Newton iterations, $\mathbf{A}$ is held constant while $\mathbf{B}$ is updated in each iteration. Since the typical number of unknowns in Eq. (4) is large (20 000–100 000), direct matrix solution techniques are not practical. We have, therefore, used the biconjugate gradient sparse matrix solution technique with incomplete LU factorization for preconditioning.[18] The particular implementation of this method that was used was developed by Greenbaum and

Seager.[19] By integrating Eqs. (1)–(3) implicitly, the allowable time step increases to the order of a nanosecond during the discharge pulse, which allows one to simulate multiple PDP pulses in a few hours on fast workstations.

Once charged species densities, the electrical potential, and charge on dielectric surfaces have been computed at a particular time, we update the density of the neutral species using

$$\frac{\partial n_i}{\partial t} - \nabla \cdot (D_i \nabla n_i) = S_i, \quad i = 1,2,...,N_{\text{neu}}, \tag{5}$$

where N_{neu} is the number of neutral species. Since the uncharged species evolve on a time scale much longer than for charged species, Eq. (5) was integrated explicitly in time. Power deposition is computed assuming Joule heating,

$$P = \nabla \phi \cdot \sum_{i=1}^{N_{\text{ch}}} [q_i(D_i \nabla n_i + (q_i/|q_i|)\mu_i n_i \nabla \phi)]. \tag{6}$$

where the term for current density contains contributions from both drift and diffusion.

Two different techniques were implemented for computing electron impact source functions and transport coefficients. The simplest and fastest is the local field approximation (LFA). Prior to running the PDP simulation, the spatially independent Boltzmann equation is solved for the electron energy distribution using a two-term spherical harmonic expansion. These distributions are used to generate a lookup table containing electron impact reaction rates, electron temperature T_e, and momentum transfer collision frequency ν_m as a function of E/N (E is the electric field strength and N is the total gas density). During the PDP simulation, reaction rate coefficients and collision frequency are obtained as a function of the local values of E/N by interpolating from the lookup table. The electron transport coefficients and source functions are computed in terms of these coefficients using the standard expressions.[20]

Although the LFA method is fast, it does not take into account the electron energy redistribution resulting from thermal conduction and convection. We, therefore, also implemented another method to generate electron transport coefficients in which the electron energy conservation equation is integrated implicitly in time to obtain the electron temperature:

$$\frac{\partial(n_e \tau)}{\partial t} = P(\tau) - n_e \sum_i N_i \kappa_i - \nabla \cdot \left(\frac{5}{2} \tau \Gamma_e - \lambda \nabla T_e\right), \tag{7}$$

where $\tau \equiv 3k_B T_e/2$, $P(\tau)$, κ_i, Γ_e, and λ are the mean electron energy, power absorbed from the electric field, power lost in collision i, electron flux, and thermal conductivity, respectively. The thermal conductivity is obtained from[21]

$$\lambda = 8n_e T_e/(\pi m_e \nu_m), \tag{8}$$

where ν_m is the electron momentum transfer collision frequency. Once the electron temperature is known, the collision frequency and reaction rate coefficients are determined by interpolating from the Boltzmann derived lookup table using electron temperature as the lookup factor.

The mobility and diffusion coefficients for ions and neutral species do not change significantly over the range of conditions of pressure and electric field of interest to PDPs. Constant values at a given pressure were therefore used for ion mobility and were obtained from Ref. 22. The diffusion coefficients for uncharged species were determined using Lennard–Jones parameters.[23]

Secondary electron emission is one of the primary processes in PDP cells which determine the breakdown voltage. Two methods were implemented to address secondary electron emission. In the simpler method, we compute the flux of all ions and excited species onto dielectric surfaces. The flux of returning secondary electrons is then given by

$$\Gamma_{\text{se}} = -\sum_i \gamma_i \Gamma_i, \tag{9}$$

where Γ_{se}, Γ_i, and γ_i are the secondary electron flux, flux of species i, and secondary electron emission coefficient for species i, respectively. Γ_{se} is then used as a boundary condition for electron flux at surfaces during the solution of Eqs. (1)–(3). We also implemented a Monte Carlo simulation (MCS) to better resolve secondary electron transport. In the MCS, pseudoparticles are launched from surfaces having secondary electron emission with initial statistical weights proportional to Γ_{se}. The trajectories and collisions of the pseudoparticles are tracked until they either collide with the walls or slow to thermal speeds.[24] The electron energy distributions of the secondary electrons as a function of position are determined, and their contributions to electron source functions are computed by convolving the distributions with the appropriate cross sections. These sources are held fixed between updates of the MCS.

The purpose of a PDP cell is to generate visible photons. The gas mixtures typically used in color PDP cells, however, produce UV radiation, which is then converted to visible light by means of phosphors. The efficiency of a PDP cell is then directly related to both the efficiency of generating UV photons and their transport to the phosphor. To evaluate this efficiency, we implemented a radiation transport model in the PDP simulation. It was not found necessary to closely couple the radiation transport with the plasma hydrodynamics as the UV and visible light radiation do not have a noticeable effect on the electrodynamics of the PDP cells under the conditions of interest. The radiation transport model is an off-line module that is invoked periodically during the simulation to compute visible light output. One can generally divide the UV photons of interest into optically thick (those that can be reabsorbed by their parent ground state atoms such as the radiation from Xe*) and optically thin (e.g., from Xe_2^* which does not have a bound or heavily populated ground state). In the radiation transport module, the source functions for UV photons are computed at all locations. For optically thick radiation, only locations within a few absorption lengths of the phosphor are considered since radiation from other locations will be readily reabsorbed. For the conditions of our simulation, Xe* UV radiation is nearly completely trapped inside the cell. Holstein[25] demonstrated that, under such a condition, radiation trapping could be taken into account by multiplying the rate coefficient for photon
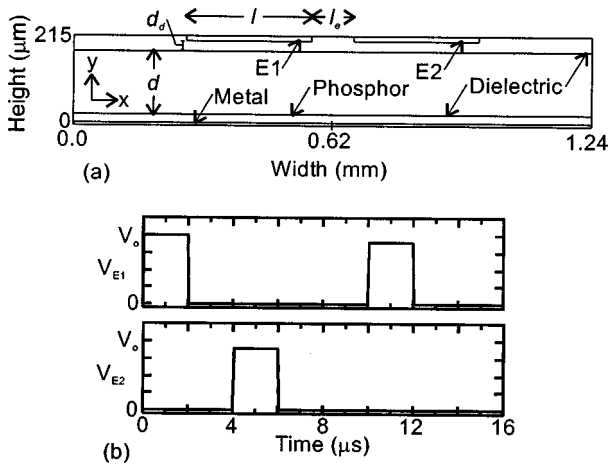
FIG. 1. (a) Schematic of the coplanar-electrode PDP cell. (b) Applied voltage on electrodes $E1$ and $E2$.

emission by an escape factor $g \sim T(\rho)$ where T is the transmission probability and ρ is the shortest dimension of the enclosure. Under the assumption of pressure broadening, g is given by[25]

$$g = \left(\frac{\lambda_0}{3\pi d} \frac{N_{\text{tot}}}{N_{\text{Xe}}} \right)^{1/2},$$ (10)

where λ_0 is the wavelength of the radiation, d is the distance between the dielectrics [Fig. 1(a)] and $N_{\text{Xe}}/N_{\text{tot}}$ is the ratio of Xe in the gas mixture. Assuming that UV photons are emitted isotropically, their fluxes onto the phosphor are computed using ray-tracing techniques. This flux is coupled with the prespecified UV-visible photon conversion efficiency in the phosphor to compute the outflux of visible photons. (It is assumed that the gas will not absorb visible radiation.) The flux of visible photons originating from the phosphor arriving on the output window is again computed using ray-tracing techniques under the assumption of Lambertian emission from the phosphor. In the results described in this article and Ref. 4, a unity quantum efficiency for UV-visible photon conversion has been assumed.

The reaction mechanism we used for He/Ne/Xe gas mixtures is shown in Table I. A seven-level model was used for Xe since it is the primary species generating UV radiation. The Xe model consists of ground state Xe, singly charged ion Xe^+, Xe^* ($6s$ states), Xe^{**} ($6s'$ states), a composite excited state Xe^{***} [nominally $Xe(6p,5d)$], the dimer excited state Xe_2^*, and the dimer ion Xe_2^+. The radiative $6s$ state is lumped into Xe^* and the radiative $6s'$ state is lumped into Xe^{**}. The proportion of Xe^* and Xe^{**} atoms in the radiative state, N_{rad}/N_*, is determined using the following expression which assumes collisional coupling between the two $6s$ or $6s'$ levels,

$$\frac{N_{\text{rad}}}{N_*} = \frac{g_r/g_m \exp(-\Delta\epsilon/k_B T_g)}{1 + g_r/g_m \exp(-\Delta\epsilon/k_B T_g)},$$ (11)

where g_r and g_m are the multiplicity of the radiative and metastable states, $\Delta\epsilon$ is the energy difference between the radiative and metastable levels, and T_g is the gas temperature. Currently, five-level models were used for Ne and He.

They consist of the ground state (Ne and He), singly charged ion (Ne^+ and He^+), a composite excited state (Ne^* and He^*), the dimer excited state (Ne_2^* and He_2^*) and the dimer ion (Ne_2^+ and He_2^+).

III. DYNAMICS OF THE COPLANAR-ELECTRODE PDP CELL

The coplanar-electrode PDP cell design[17] has been widely adopted by the display industry. Although the discharge operation is more complicated, the coplanar geometry offers several advantages over the opposing-electrode design. For example, phosphors are subjected to less bombardment by energetic ions, which prolongs the phosphor life. In this section, we describe the operation of the coplanar-electrode PDP cell using He/Ne/Xe gas mixtures. The generic cell geometry is shown in Fig. 1(a). The PDP cell consists of two upper transparent electrodes, $E1$ and $E2$, which are separated from the gas by a dielectric. The bottom of the cell consists of a dielectric with a phosphor coating on top and a metal address electrode below which is kept at ground potential for these results. The permittivities of the top and bottom dielectrics are $\epsilon/\epsilon_0 = 15$ and 10, respectively, and they are separated by 150 μm. Barrier ribs were not included since they are typically in the plane that is not resolved in these 2D simulations. Reflective boundary conditions at the lateral ends, $x = 0$ and 1.24 mm, were used. The top dielectric, $E1$ and $E2$ are transparent to visible photons, allowing light to be emitted from the top of the cell. The surfaces of both dielectrics are coated with a material having a high rate of secondary electron emission. The voltage pulses applied to $E1$ and $E2$ with amplitude V_0 are shown in Fig. 1(b). All rise and fall times are 20 ns.

The operation of the coplanar-electrode PDP cell sustained in He/Ne/Xe = 70/26/4 at 400 Torr and $V_0 = 200$ V is shown in Figs. 2–10. The cycle starts with zero potential on $E1$ and $E2$ and a negligible density of charged species. Starting at 10 ns, the voltage at electrode $E1$ is increased to 200 V in 20 ns. The electrical potential, electron density, and charge on dielectric surfaces at different times during the subsequent discharge are shown in Figs. 2–4.

At 50 ns, the discharge has just initiated and the electrical potential [Fig. 2(a)] is characteristic of vacuum fields. The electron density at 50 ns [Fig. 3(a)] is small and electrons are mainly generated by ionization below $E1$ where the electric field is the largest. The charge on the surfaces of the dielectrics (Fig. 4) is negligible. Positive ions generated in the discharge drift towards the grounded electrodes ($E2$ and the address electrode) under the influence of the applied electric field, where secondary electrons are generated when ions bombard the dielectric surfaces. As the electron and ion densities increase, contributions from secondary electrons play a larger role in the discharge dynamics and eventually lead to gas breakdown (a sharp rise in electron density) around 85 ns. The electrical potential and electron density after the breakdown (100 ns) are shown in Figs. 2(b) and 3(b), respectively. The peak in electron density has shifted towards the bottom dielectric since secondary electron emission mainly takes place from that surface during the first pulse. The newly generated ions and electrons drift towards the dielec-

TABLE I. He/Ne/Xe reaction mechanisms.

Reaction	Rate[a]	References	Reaction	Rate[a]	References
Electron impact excitation and de-excitation:			**Three-body heavy particle collisions:**		
$e+Xe \rightarrow Xe^*+e$	b	26	$Xe^*+Xe+Xe \rightarrow Xe_2^*+Xe$	5.0×10^{-32} cm^6 s^{-1}	41
$e+Xe \rightarrow Xe^{**}+e$	b	27	$Xe^*+Xe+Ne \rightarrow Xe_2^*+Ne$	1.6×10^{-32} cm^6 s^{-1}	42
$e+Xe \rightarrow Xe^{***}+e$	b	28	$Xe^*+Xe+He \rightarrow Xe_2^*+He$	1.4×10^{-32} cm^6 s^{-1}	30
$e+Xe^* \rightarrow Xe+e$	b	29	$Xe^{**}+Xe+Xe \rightarrow Xe_2^*+Xe$	5.0×10^{-32} cm^6 s^{-1}	41
$e+Xe^{**} \rightarrow Xe+e$	b	c, 27	$Xe^{**}+Xe+Ne \rightarrow Xe_2^*+Ne$	1.6×10^{-32} cm^6 s^{-1}	d, 42
$e+Xe^{***} \rightarrow Xe+e$	b	c, 28	$Xe^{**}+Xe+He \rightarrow Xe_2^*+He$	1.4×10^{-32} cm^6 s^{-1}	d, 30
$e+Xe^* \rightarrow Xe^{***}+e$	b	29	$Xe^{***}+Xe+Xe \rightarrow Xe_2^*+Xe$	5.0×10^{-32} cm^6 s^{-1}	41
$e+Xe^{***} \rightarrow Xe^*+e$	b	c, 29	$Xe^{***}+Xe+Ne \rightarrow Xe_2^*+Ne$	1.6×10^{-32} cm^6 s^{-1}	d, 42
$e+Xe^* \rightarrow Xe^{***}+e$	$5.5 \times 10^{-7} T_e^{0.79} \exp(-2.0/T_e)$	30	$Xe^{***}+Xe+He \rightarrow Xe_2^*+He$	1.4×10^{-32} cm^6 s^{-1}	d, 30
$e+Ne \rightarrow Ne^*+e$	b	31	$Xe^++Xe+Xe \rightarrow Xe_2^++Xe$	2.5×10^{-31} cm^6 s^{-1}	42
$e+Ne^* \rightarrow Ne+e$	b	c, 31	$Xe^++Xe+Ne \rightarrow Xe_2^++Ne$	1.5×10^{-31} cm^6 s^{-1}	42
$e+He \rightarrow He^*+e$	b	32	$Xe^++Xe+He \rightarrow Xe_2^++He$	1.0×10^{-31} cm^6 s^{-1}	d, 42
$e+He^* \rightarrow He+e$	b	c, 32	$Ne^*+Ne+Xe \rightarrow Ne_2^*+Xe$	8.0×10^{-34} cm^6 s^{-1}	30
			$Ne^*+Ne+Ne \rightarrow Ne_2^*+Ne$	4.0×10^{-34} cm^6 s^{-1}	42
Electron impact ionization and recombination:			$Ne^*+Ne+He \rightarrow Ne_2^*+He$	1.0×10^{-34} cm^6 s^{-1}	30
$e+Xe \rightarrow Xe^++e+e$	b	33			
$e+Xe^* \rightarrow Xe^++e+e$	b	29	**Three-body heavy particle collisions:**		
$e+Xe^{**} \rightarrow Xe^++e+e$	$1.56 \times 10^{-7} T_e^{0.71} \exp(-2.63/T_e)$	30	$Ne^++Ne+Xe \rightarrow Ne_2^++Xe$	8.0×10^{-32} cm^6 s^{-1}	30
$e+Xe^{***} \rightarrow Xe^++e+e$	b	29	$Ne^++Ne+Ne \rightarrow Ne_2^++Ne$	4.4×10^{-32} cm^6 s^{-1}	38
$e+Xe_2^+ \rightarrow Xe_2^++e+e$	$9.75 \times 10^{-8} T_e^{0.71} \exp(-3.4/T_e)$	30	$Ne^++Ne+He \rightarrow Ne_2^++He$	3.0×10^{-32} cm^6 s^{-1}	43
$e+Xe_2^+ \rightarrow Xe^*+Xe$	b	34	$He^*+He+Xe \rightarrow He_2^*+Xe$	8.0×10^{-3} cm^6 s^{-1}	30
$e+Xe_2^+ \rightarrow Xe^{**}+Xe$	$3.33 \times 10^{-7} T_e^{-0.5}$	35	$He^*+He+Ne \rightarrow He_2^*+Ne$	4.0×10^{-33} cm^6 s^{-1}	30
$e+Xe_2^+ \rightarrow Xe^{***}+Xe$	$3.7 \times 10^{-8} T_e^{-0.5}$	35	$He^*+He+He \rightarrow He_2^*+He$	1.3×10^{-33} cm^6 s^{-1}	30
$e+Ne \rightarrow Ne^++e+e$	b	33	$He^++He+Xe \rightarrow He_2^*+Xe$	5.0×10^{-32} cm^6 s^{-1}	30
$e+Ne^* \rightarrow Ne^++e+e$	b	36	$He^++He+Ne \rightarrow He_2^++Ne$	7.0×10^{-32} cm^6 s^{-1}	30
$e+Ne_2^+ \rightarrow Ne_2^++e+e$	$9.75 \times 10^{-9} T_e^{0.71} \exp(-3.4/T_e)$	30	$He^++He+He \rightarrow He_2^++He$	1.0×10^{-31} cm^6 s^{-1}	30
$e+Ne_2^+ \rightarrow Ne^*+Ne$	$3.7 \times 10^{-8} T_e^{-0.5}$	35	$Ne^*+Xe+Xe \rightarrow Xe_2^*+Ne$	1.0×10^{-33} cm^6 s^{-1}	30
$e+He \rightarrow He^++e+e$	b	36			
$e+He^* \rightarrow He^++e+e$	b	36	**UV radiation:**		
$e+He_2^* \rightarrow He_2^++e+e$	$9.75 \times 10^{-10} T_e^{0.71} \exp(-3.4/T_e)$	30	$Xe_2^* \rightarrow Xe+Xe+h\nu$	7.22×10^7 s^{-1}	44
$e+He_2^+ \rightarrow He^*+He$	$5.0 \times 10^{-9} T_e^{-0.5}$	37	$Ne_2^* \rightarrow Ne+Ne+h\nu$	7.50×10^7 s^{-1}	42
			$Xe_r^* \rightarrow Xe+h\nu$	2.9×10^8 g s^{-1}	e, 25, 45
Two-body heavy particle collisions:			$Xe_r^{**} \rightarrow Xe+h\nu$	4.05×10^8 g s^{-1}	e, 25, 45
$Xe^*+Xe^* \rightarrow Xe^++Xe+e$	5.0×10^{-10}	38			
$Xe^{**}+Xe^{**} \rightarrow Xe^++Xe+e$	5.0×10^{-10}	d, 38			
$Xe^{***}+Xe^{***} \rightarrow Xe^++Xe+e$	5.0×10^{-10}	d, 38			
$Ne^*+Ne^* \rightarrow Ne^++Ne+e$	1.0×10^{-11}	30			
$He^*+He^* \rightarrow He^++He+e$	2.7×10^{-10}	39			
$Ne^++Xe \rightarrow Ne+Xe^+$	1.0×10^{-11}	30			
$Ne^*+Xe \rightarrow Xe^++Ne+e$	1.0×10^{-10}	30			
$He^*+Xe \rightarrow Xe^++He+e$	7.5×10^{-11}	30			
$Ne_2^++Xe \rightarrow Xe^++Ne+Ne$	1.0×10^{-10}	30			
$He_2^++Xe \rightarrow Xe^++He+He$	1.0×10^{-12}	30			
$He_2^++Ne \rightarrow Ne^++He+He$	6.0×10^{-10}	40			
$He_2^*+Xe \rightarrow Xe^++He+He+e$	5.0×10^{-10}	30			
$He_2^*+Ne \rightarrow Ne^++He+He+e$	1.0×10^{-11}	30			
$Ne_2^*+Xe \rightarrow Xe^++Ne+Ne+e$	7.5×10^{-11}	30			

[a]Units are cm^3 s^{-1} unless stated otherwise. T_e is the electron temperature (eV).
[b]Determined as a function of the electron temperature T_e or the local value of E/N from the lookup table obtained from the solution of the Boltzmann equation.
[c]Computed through detailed balance using data from the specified reference.
[d]Estimated using data from the specified reference.
[e]g is a radiation trapping factor defined in Sec. II. Xe_r^* is the fraction of Xe* in radiative states.

trics where they are collected, thereby charging their capacitance. The resulting potential drop across the dielectrics reduces the voltage across the gas gap, which can be seen in the potential profile at 100 ns [Fig. 2(b)]. As the potential drop across the gas gap is reduced below the threshold for sustaining the discharge, the discharge is quenched and the electron density rapidly decreases [Fig. 3(c)]. The surface

charge profiles [Fig. 4(a)] show that positive ions have dominantly charged the bottom dielectric while the top dielectric surface has primarily been negatively charged. Once the discharge has been quenched, the gas remains electrically inactive until the next pulse. However, as we will show later on, the cell emits visible light for a considerably longer time than the discharge. When the voltage at $E1$ is brought down

to 0 V at around 2 μs, a significant voltage drop remains across the gas gap due to the charge on the dielectric surfaces.

Starting at 4.01 μs, the voltage on $E2$ is increased to 180 V in 20 ns [Fig. 1(b)], which initiates another discharge whose dynamics are shown in Figs. 4(b) and 5–8. At 4.05 μs, the discharge has just started and the electrical potential [Fig. 5(a)] is similar to that in vacuum, albeit with charged dielectrics. The negative charge under $E1$ adds to the voltage across the gap making it larger than that due to the external supply. The electron density at 4.05 μs [Fig. 6(a)] is small enough that the volumetric space charge does not significantly alter the applied fields. The electrons are, therefore, almost freely accelerated towards the positively biased electrode $E2$. The Xe^+ density at 4.05 μs [Fig. 7(a)] is also small, and the ions are displaced from the electrons as the ions drift towards $E1$ and space charge is insufficient to maintain charge neutrality. This behavior is different from the first pulse because the negative surface charge under $E1$ produces an additional attractive electric field for the positive ions, while the positive charge on the bottom dielectric sets up a field which repels the positive ions. Similar to the first pulse, secondary electron emission promotes breakdown and the electron density rises sharply as shown in Fig. 6(b) at 4.1 μs. At this time, the plasma density is sufficiently large to require charge neutrality. During the second pulse, the discharge is initially between the adjacent corners of $E1$ and $E2$ because the electric field is the largest there. As the potential drop at the corners decreases due to charge build up on the dielectric surfaces, the discharge shifts towards the outer edges of the electrodes. Eventually, the whole dielectric surface under $E2$ charges up and the discharge is quenched. As can be seen by comparing the electron and Xe^+ densities in Figs. 6(c) and 7(c), ion charging of surfaces and their decay in density is slower than that for electrons after the plasma density decays below the ambipolar limit. This is because the ion mobility is smaller than the electron mobility.

The charge on the top and bottom dielectrics for the second pulse is shown in Fig. 4(b). Before the discharge starts (4.05 μs), there is a small positive charge underneath $E2$ left from the first pulse. Electrons produced during the

second pulse negatively charge the dielectric under $E2$. Similarly, the ions charge the dielectric underneath $E1$ and reverse the charge polarity there. As the pulse progresses the charging spreads laterally, an indication of the spreading of the discharge. Some of the ions also charge the bottom dielectric, producing even stronger repelling electric fields for positive ions during the subsequent pulses.

The purpose of the PDP cell is to generate visible light. In the Xe reaction chemistry, the main species which produce phosphor-exciting UV photons are Xe^*, Xe^{**}, and Xe_2^*. The densities of Xe^* and Xe_2^* are shown in Fig. 8 at 4.1 μs, the time when electron density is close to its peak. Xe^* density is the sum of the $6s$ radiative and metastable states. The Xe^* and Xe_2^* peak densities are physically located close to the region of peak electron density. Xe^* is mainly produced by electron impact excitation (secondarily by dissociative recombination of Xe_2^+) and is quenched by superelastic collisions and generation of Xe_2^* through collisions with Xe and a stabilizing third body. Since the radiative decay of Xe_2^* is rapid, its density is considerably smaller than the Xe^* density at 4.1 μs. We will, however, show later that Xe_2^* contribution to phosphor excitation is larger.

When the electron density is close to its peak value during the discharge, the electric fields (or E/N) within the plasma settle down to the minimum required for sustaining the discharge. A distinct cathode fall can be observed at this stage near the negatively biased electrodes [Figs. 2(b) and 5(b)]. Since electric fields are largest at these locations, most of the power deposition (approximately proportional to E^2) takes place there, as shown at 4.1 μs in Fig. 8(c). Power is mainly being deposited below $E1$, where secondary electrons are generated through ion bombardment. The power deposition scenario is not necessarily the optimum from the light generation efficiency perspective. Excitation of Xe takes place near the top dielectric which is far from the phosphor. The UV emission is, therefore, not converted to visible light efficiently. Also since the voltage pulse is longer than the RC time constant to charge the dielectric, most of the excitation
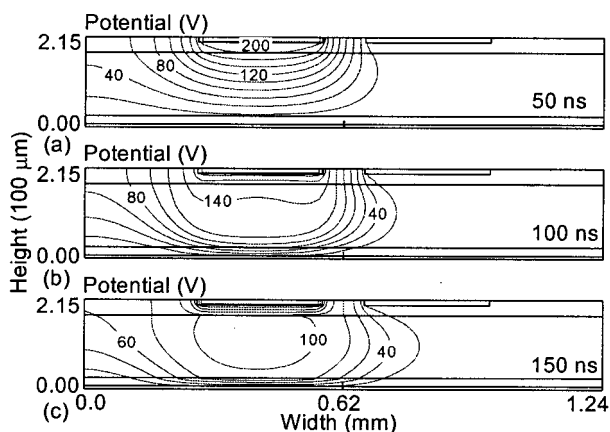

FIG. 2. Evolution of electrical potential during the first pulse when V_{E1} = 200 V, V_{E2} = 0 V. (a) 50, (b) 100, and (c) 150 ns.
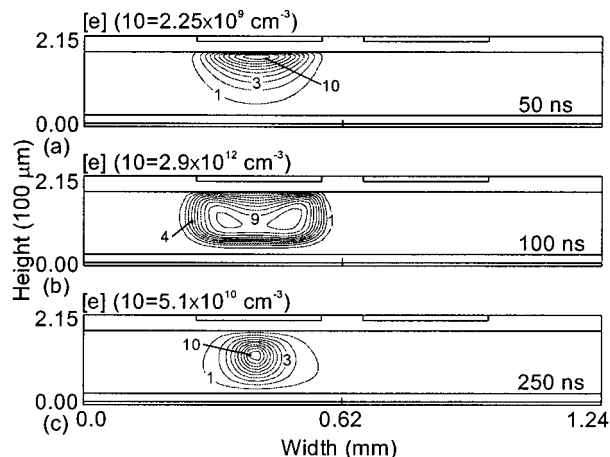

FIG. 3. Evolution of electron density during the first pulse when V_{E1} = 200 V, V_{E2} = 0 V. (a) 50, (b) 100, and (c) 250 ns. Contours are labeled 0–10, with 10 corresponding to the maximum density.
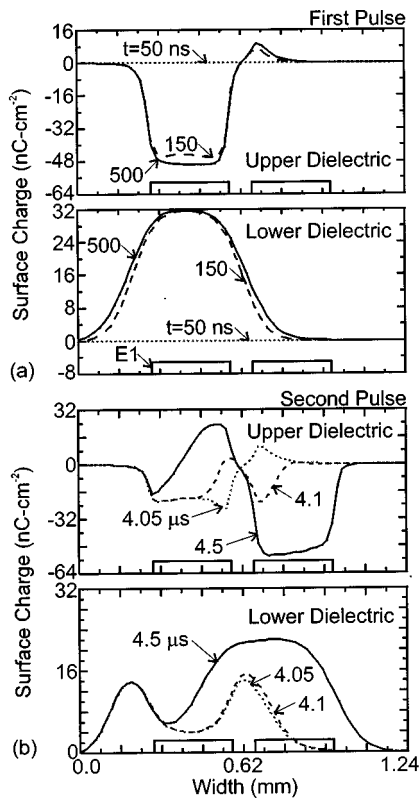
FIG. 4. Accumulated charge on the surface of the upper and lower dielectrics. (a) During the first pulse when $V_{E1} = 200$ V, $V_{E2} = 0$ V. (b) During the second pulse when $V_{E1} = 0$ and $V_{E2} = 180$ V.

occurs during the positive column phase at low E/N and low efficiency. As we discuss in Ref. 4, PDP efficiency can be improved within limits by minimizing the duration of the discharge.

Coplanar electrode PDP cells are generally operated by next applying the first voltage pulse to $E1$ [Fig. 1(b)], and repeating the second and third pulse alternately to $E2$ and $E1$ as long as required. When a third pulse of 180 V is applied to $E1$, the same processes that occurred during the second pulse take place, but in the opposite direction. For example, the electric potential, electron density and Xe^+
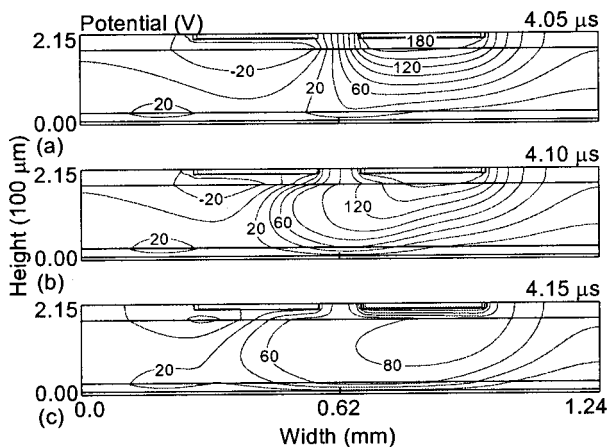

FIG. 5. Evolution of electrical potential during the second pulse when $V_{E1} = 0$ V, $V_{E2} = 180$ V. (a) 4.05, (b) 4.10, and (c) 4.15 μs.
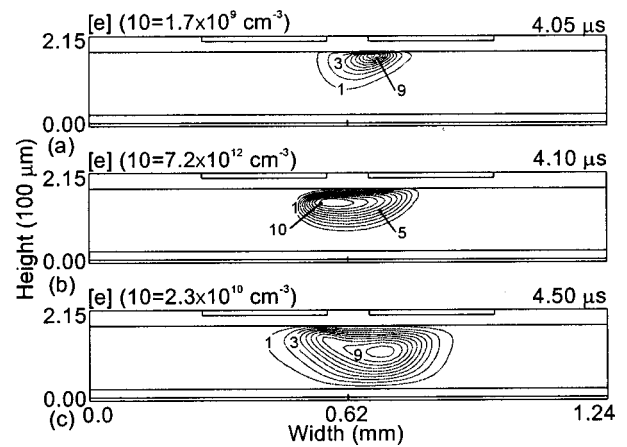

FIG. 6. Evolution of electron density during the second pulse when $V_{E1} = 0$ V, $V_{E2} = 180$ V. (a) 4.05, (b) 4.10, and (c) 4.15 μs. Contours are labeled 0–10, with 10 corresponding to the maximum density.

density during the third pulse are shown in Fig. 9 at 10.1 μs. The electrons drift towards $E1$ and ions mainly drift towards $E2$. Although there are some variations in species density and surface charge in subsequent pulses, the device achieves a quasisteady state in only a few cycles.

The characteristics of excited-state Xe species that generate optically thick UV radiation (Xe^* and Xe^{**}) and optically thin radiation (Xe_2^*) are generally different. Xe^* is primarily generated by electron impact excitation and secondarily by dissociative recombination of Xe_2^+, and its density decays through electron impact deexcitation during the pulse, three-body collisions, radiative decay, and most slowly by diffusion to the walls. On the other hand, Xe_2^* is produced by three-body collisions, and radiative decay is the primary loss process with a minor loss from diffusion. As shown in Fig. 8(b), the Xe^* (and Xe^{**}) density increases rapidly during the discharge phase when electron density is large. The Xe_2^* density, however, increases more slowly and, because of its short lifetime, never becomes larger than
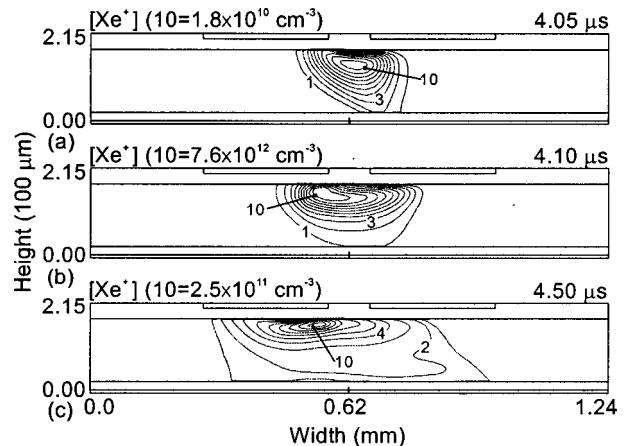

FIG. 7. Evolution of Xe^+ density during the second pulse when $V_{E1} = 0$ V, $V_{E2} = 180$ V. (a) 4.05, (b) 4.10, and (c) 4.15 μs. Contours are labeled 0–10, with 10 corresponding to the maximum density.
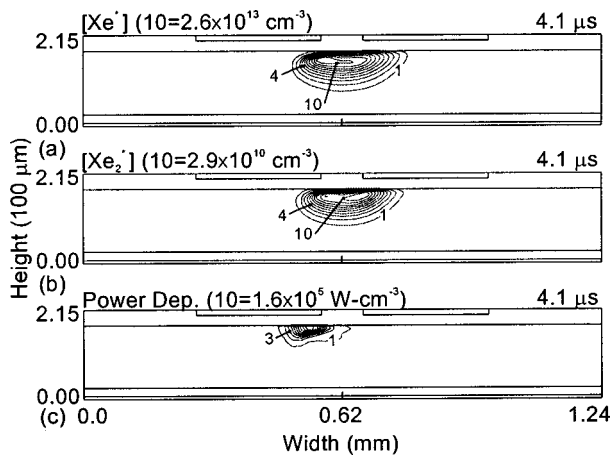
FIG. 8. Discharge characteristics at 4.1 μs during the second pulse when $V_{E1}=0$ V, $V_{E2}=180$ V. (a) Xe* density, (b) Xe$_2^*$ density, and (c) power deposition. Contours are labeled 0–10, with 10 corresponding to the maximum density.
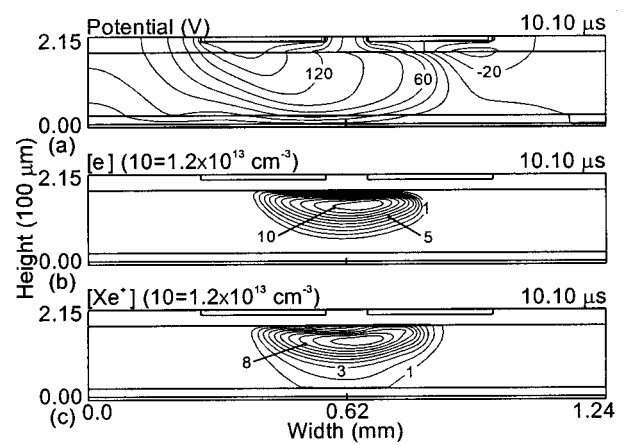
FIG. 9. Discharge characteristics at $t=10.1$ μs during the third pulse when $V_{E1}=180$ V, $V_{E2}=0$ V. (a) Electrical potential, (b) electron density, and (c) Xe$^+$ density. Contours are labeled 0–10, with 10 corresponding to the maximum density.

10^{12} cm^{-3}. After the discharge has been quenched, Xe metastable states act as a reservoir which keeps pumping energy into generating Xe$_2^*$ for many microseconds, increasing the effective lifetime of Xe$_2^*$ in the cell. In addition to the differences in lifetimes, UV radiation from only those Xe* (and Xe**) atoms that are within a few absorption wavelengths of the phosphor (5–10 μm) is useful for visible light generation. On the other hand, UV radiation from Xe$_2^*$ is optically thin and photons generated anywhere in the cell can reach the phosphors and produce visible light. Due to these differences in temporal and spatial scales, Xe$_2^*$ molecules contribute more strongly to visible light emission than Xe* and Xe** for this geometry and operating conditions. For example, the total fluence of visible light photons as a function of position across the top of the cell generated during the second pulse (4–10 μs) is shown in Fig. 10(a). Phosphor generated photons due to UV emission from the dimer state (Xe$_2^*$) and from Xe excited states (Xe* and Xe**) are compared. The dimer contribution to visible light is substantially larger than that due to the excited states of Xe.

Since Xe metastables (and hence the dimers they generate) survive for a substantial time after the discharge has been quenched, one can obtain visible light from the cell for many microseconds. This is illustrated in Fig. 10(b) where the visible light emission from the cell as a function of position is shown at different times during the second pulse. The emission has an amplitude about 25% of the peak (4.25 μs) at 10 μs. The long decay in UV light generation has recently been experimentally observed by Jeong et al.[46] Since little energy is consumed after the discharge has been quenched and the cell emits visible light for a considerably longer time, the interpulse period should be as long as practical, a practice that should translate into better efficiency. One of the many ways PDP cell efficiency can be improved is to choose operating conditions that channel more energy towards Xe$_2^*$. This can, for example, be accomplished by operating the PDP at higher pressures, which makes the three-body collision processes more efficient.[4]

Secondary electrons emitted from surfaces are acceler-

ated by the large electric field in the sheath regions. Even at a few hundred Torr pressure, the secondary electrons are not in equilibrium with the field and have beam-like characteristics, thermalizing after several energy loss collisions. To better resolve the dynamics of secondary electrons before they thermalize, a Monte Carlo simulation was implemented in the PDP model. The surface charge and visible light output with and without the MCS are shown in Fig. 11 for the base case conditions. Without the MCS, all secondary electrons are launched at the dielectric surface where the E/N is large near the edge of $E1$. Ionization occurs in the same region of large E/N, leading to rapid avalanches. However, when the MCS is used, some of the secondary electrons produce ionizations and thermalize farther from the region of large E/N and so secondary electrons do not rapidly avalanche on the top surface. Consequently, the source functions for electron impact reactions are over-estimated in the preavalanche stage in the absence of the MCS and the discharge is initiated earlier. This is demonstrated in Fig. 11(a) using charge on top dielectric surface at 4.1 μs as an indicator. In the result without the MCS, the discharge has been initiated earlier and surface charge has evolved farther towards the final state shown in Fig. 11(b). Even though the detailed dynamics of the discharge are different for the two cases, the charge on the top dielectric surface after the discharge [Fig. 11(b)] and total visible light emission during the second cycle [Fig. 11(c)] are similar. This result is a consequence of the minimum voltage for discharge self-sustenance being particularly sensitive to whether the MCS is used. The gap voltage is reduced to the self-sustaining voltage by dielectric charging, which is largely a property of bulk flow of current. Since the total current fluence is approximately the same for the two cases, total visible light emission is also not much effected by the MCS. These results are in agreement with those of Punset et al.[15]

If the LFA is used, the electron temperature T_e is largest in the cathode fall regions where E/N is large, and T_e is very small in the plasma region where E/N is close to the minimum necessary for sustaining the discharge. Electron energy
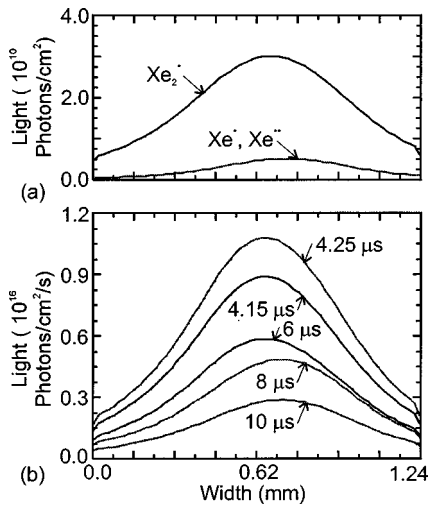
FIG. 10. Visible light characteristics for the second pulse as a function of position across the top of the cell ($V_{E1} = 0$ V, $V_{E2} = 180$ V). (a) Contributions of Xe dimer state (Xe_2^*) and Xe excited states (Xe^* and Xe^{**}) to total visible light fluence during the second cycle (4–10 μs). (b) Visible flux during the second pulse.

FIG. 11. Discharge properties with and without the MCS. (a) Charge on upper dielectric surface at 4.1 μs, (b) charge on upper dielectric surface at 6.0 μs, and (c) total visible photons emitted between 4–6 μs from the top of the cell. $V_{E1} = 0$ V, $V_{E2} = 180$ V.

redistribution can, however, take place due to thermal conduction and convection sufficient to change the discharge dynamics considerably. To take account of this energy redistribution and its consequences on the discharge characteristics, we self-consistently compute T_e in the PDP model by solving the electron energy conservation equation.

To demonstrate the consequences of electron energy redistribution on the PDP dynamics, T_e during the discharge and charge on the upper dielectric surface after the discharge (4.5 μs) are shown in Fig. 12 for cases using the LFA and the electron energy equation (EEE). (During avalanche, the EEE predicts a higher electron temperature in the bulk plasma, and so the discharge is initiated earlier. We have, therefore, compared T_e for the two cases at different times when the discharges are approximately in the same stage of development.) With the LFA, the electron temperature is largest below $E1$, about 9 eV, where the cathode fall is located [Fig. 12(a)]. Since E/N in the bulk plasma is smaller near $E2$, T_e is smaller there as well, ~4 eV. When the EEE is used for T_e, the electron temperature in the cathode fall region reduces to <5 eV because of electron energy transport by conduction and convection to colder regions of the cell [Fig. 12(b)]. T_e, increases in the bulk plasma below $E2$ (relative to the cathode fall region) because of thermal conduction and the drift of warm electrons from the cathode fall region.

Once the discharge has been initiated, most of the electron impact ionization takes place adjacent to the cathode fall. The EEE predicts a smaller T_e there than does the LFA because energy is transported to the colder positive column region. Source functions for electron impact ionization reactions are, therefore, smaller for the case using the EEE and the discharge is quenched earlier. This is demonstrated in Fig. 12(c) where the charge on top dielectric surface is compared for the two cases after the discharge has been extinguished. Since the discharge is sustained for a shorter period when T_e is obtained from the EEE, less dielectric surface
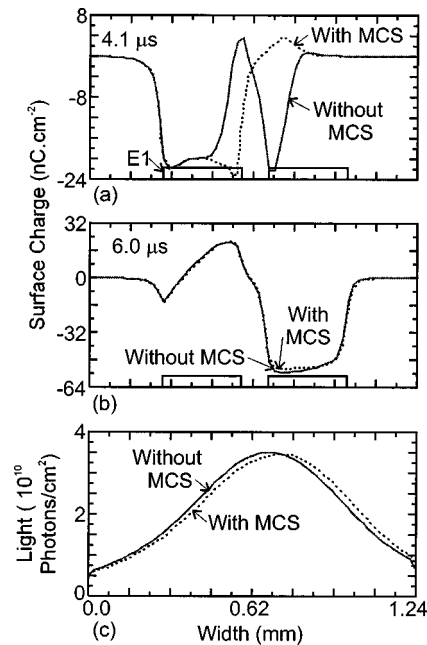
charging takes place. Although T_e generally behaves in the same manner as described above, the details of discharge dynamics may be different for other operating conditions. Self-consistent computation of T_e is, however, found to substantially change the discharge characteristics.

IV. CONCLUDING REMARKS

In this article, results from a 2D hybrid simulation for PDPs were used to investigate operation of a coplanar-electrode PDP cell using He/Ne/Xe gas mixtures. The dimensions of the PDP cell were such that the first voltage pulse produced a discharge between the powered electrode and the bottom address electrode, which was grounded. Due to the charging of the dielectrics, the discharge shifted to being between the coplanar electrodes from the second pulse onward. In the Xe based reaction chemistry, UV photons are generated by the excited states of Xe (Xe^* and Xe^{**}) and the Xe dimer (Xe_2^*). Although the Xe_2^* density was considerably smaller than the density of Xe^* or Xe^{**} during the discharge phase due to its short lifetime, Xe_2^* was found to contribute more strongly to total visible light emission for the conditions examined. This is because the UV radiation from Xe_2^* is optically thin and photons produced in any part of the cell can reach the phosphor. Also Xe metastables readily convert to Xe_2^* due to three body collisions.

Two methods were implemented in the PDP model to better resolve the details of electron dynamics as compared to LFA. The Monte Carlo simulation improves upon the representation of the secondary electrons during the stage prior to thermalization. It was found that the discharge occurs later because the electron impact source functions are overestimated during the early stages of discharge buildup if the MCS is not used. The MCS, however, does not significantly
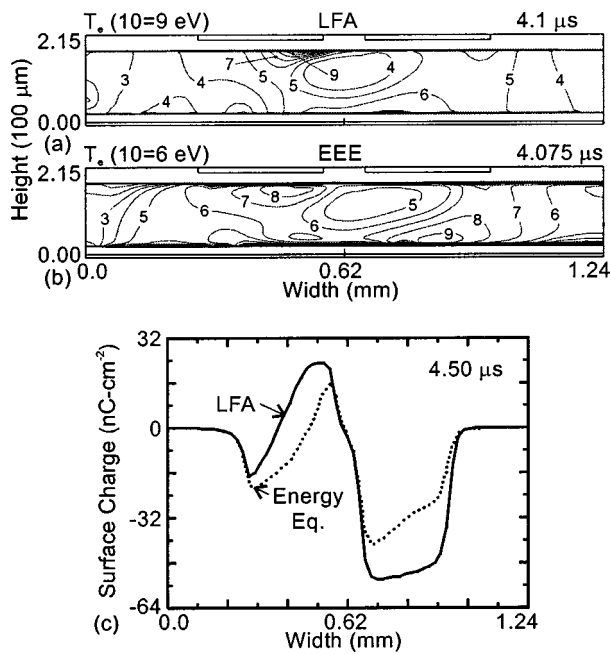
FIG. 12. Discharge properties using the LFA and electron energy equation to compute T_e. (a) Electron temperature (T_e) using the LFA, (b) T_e obtained with the electron energy equation, and (c) charge on upper dielectric surface at 4.50 μs. $V_{E1}=0$ V, $V_{E2}=180$ V.

effect the minimum voltage for discharge self-sustenance, total current fluence during the discharge, accumulated charge on dielectric surfaces and total visible light emission. When the electron temperature is self-consistently computed by solving the electron energy conservation equation, T_e is larger in the bulk plasma region (compared to the cathode fall region) than that is predicted by LFA due to energy gain through thermal conduction and convection. These changes in T_e in the different regions of the discharge modify the discharge initiation time and the overall discharge characteristics.

ACKNOWLEDGMENTS

[1] A. Sobel, IEEE Trans. Plasma Sci. **19**, 1032 (1991); A. Sobel, Sci. Am. **278**, 70 (1998).

[2] *Electronic Display Devices*, edited by S. Matsumoto (Wiley, New York, 1990), p. 131.

[3] J. A. Castelano, *Handbook of Display Technology* (Academic, New York, 1992), p. 111.

[4] S. Rauf and M. J. Kushner, J. Appl. Phys. **85**, 3470 (1999).

[5] D. L. Bitzer and H. G. Slottow, Proceedings of the AFIPS Conference **29**, 541 (1966).

[6] O. Sahni, C. Lanza, and W. E. Howard, J. Appl. Phys. **49**, 2365 (1978).

[7] O. Sahni and C. Lanza, J. Appl. Phys. **47**, 1337 (1976).

[8] O. Sahni and C. Lanza, J. Appl. Phys. **47**, 5107 (1976).

[9] R. B. Campbell, R. Veerasingam, and R. T. McGrath, IEEE Trans. Plasma Sci. **23**, 698 (1995).

[10] R. Veerasingam, R. B. Campbell, and R. T. McGrath IEEE Trans. Plasma Sci. **23**, 688 (1995).

[11] R. Veerasingam, R. B. Campbell, and R. T. McGrath, Plasma Sources Sci. Technol. **6**, 157 (1997).

[12] P. J. Drallos, V. P. Nagorny, and W. Williamson, Phys. Scr. **T53**, 75 (1994).

[13] P. J. Drallos, V. P. Nagorny, and W. Williamson, Plasma Sources Sci. Technol. **4**, 576 (1995).

[14] J. P. Boeuf and L. C. Pitchford, IEEE Trans. Plasma Sci. **24**, 95 (1996).

[15] C. Punset, J. P. Boeuf, and L. C. Pitchford, J. Appl. Phys. **83**, 1884 (1998).

[16] H. G. Slottow, IEEE Trans. Electron Devices **23**, 760 (1976).

[17] S. Sato, H. Yamamoto, Y. Shirochi, I. Iemori, N. Nakayama, and I. Morita, IEEE Trans. Electron Devices **23**, 328 (1976).

[18] M. K. Seager, LLNL Technical Report UCRL-100195 (1988).

[19] SLAP sparse matrix library. Available at Oak Ridge National Laboratory's numerical subroutines archive NETLIB (http://www.netlib.org).

[20] M. A. Lieberman and A. J. Lichtenberg, *Principles of Plasma Discharges and Materials Processing* (Wiley, New York, 1994), p. 129.

[21] M. Mitchner and C. H. Kruger, Jr., *Partially Ionized Gases* (Wiley, New York, 1973), p. 92.

[22] H. W. Ellis, R. Y. Pai, E. W. McDaniel, E. A. Mason, and L. A. Viehland, At. Data Nucl. Data Tables **17**, 177 (1976); H. W. Ellis, E. W. McDaniel, D. L. Albritton, L. A. Viehland, S. L. Lin, and E. A. Mason, At. Data Nucl. Data Tables **22**, 179 (1978); H. W. Ellis, M. G. Thackston, E. W. McDaniel, and E. A. Mason, At. Data Nucl. Data Tables **31**, 113 (1984); L. A. Viehland and E. A. Mason, At. Data Nucl. Data Tables **60**, 37 (1995).

[23] J. O. Hirschfelder, C. F. Curtiss, and R. B. Bird, *Molecular Theory of Gases and Liquids* (Wiley, New York, 1954), p. 539.

[24] Y. Weng and M. J. Kushner, Phys. Rev. A **42**, 6192 (1990).

[25] T. Holstein, Phys. Rev. **72**, 1212 (1947); T. Holstein, Phys. Rev. **83**, 1159 (1951).

[26] N. J. Mason and W. R. Newell, J. Phys. B **20**, 1357 (1987).

[27] T. Y. Suzuki, Y. Sakai, B. S. Min, T. Takayanagi, K. Wakiya, H. Suzuki, T. Inaba, and H. Takuma, Phys. Rev. A **43**, 5867 (1991).

[28] M. Hayashi, J. Phys. D **16**, 581 (1983).

[29] D. J. Eckstrom, H. H. Nakano, D. C. Lorents, T. Rothem, J. A. Betts, M. E. Lainhart, D. A. Dakin, and J. A. Maenchen, J. Appl. Phys. **64**, 1679 (1988).

[30] J. W. Shon, Ph.D. thesis, University of Illinois, 1993.

[31] P. J. O. Teubner, J. L. Riley, M. C. Tonkin, J. E. Furst, and S. J. Buckman, J. Phys. B **18**, 3641 (1985).

[32] J. P. Boeuf and E. Marode, J. Phys. D **15**, 2169 (1982).

[33] D. Rapp and P. Englander-Golden, J. Chem. Phys. **43**, 1464 (1965).

[34] J. Bretagne, J. Godart, and V. Puech, J. Phys. D **15**, 2205 (1982).

[35] Y. J. Shui and M. A. Biondi, Phys. Rev. A **17**, 868 (1978).

[36] L. Vriens, Phys. Lett. **8**, 260 (1964).

[37] C. B. Collins and F. W. Lee, J. Chem. Phys. **68**, 1391 (1978).

[38] H. Hokazono, K. Midorikawa, M. Obara, and T. Fujioka, J. Appl. Phys. **56**, 680 (1984).

[39] R. Deloche, P. Monchicourt, M. Cheret, and F. Lambert, Phys. Rev. A **13**, 1140 (1976).

[40] D. K. Bohme, N. G. Adams, M. Museman, D. B. Dunkin, and E. E. Ferguson, J. Chem. Phys. **52**, 5094 (1970).

[41] M. Ohwa, T. J. Moratz, and M. J. Kushner, J. Appl. Phys. **66**, 5131 (1989).

[42] L. A. Levin, S. E. Moody, E. L. Klosterman, R. E. Center, and J. J. Ewing, IEEE J. Quantum Electron. **17**, 2282 (1981).

[43] G. E. Veach and H. J. Oskam, Phys. Rev. A **2**, 1422 (1970).

[44] F. Kinnari, A. Suda, M. Obara, and T. Fujioka, IEEE J. Quantum Electron. **19**, 1587 (1983).

[45] M. Aymar and M. Coulombe, At. Data Nucl. Data Tables **21**, 537 (1978).

[46] H. S. Jeong, J. H. Seo, C. K. Yoon, J. K. Kim, and K. W. Whang, IEEE Trans. Plasma Sci. (to be published).